

Baroclinic Wave Breaking and the Internal Variability of the Tropospheric Circulation

J. G. ESLER AND P. H. HAYNES

*Centre for Atmospheric Science, Department of Applied Mathematics and Theoretical Physics,
University of Cambridge, Cambridge, United Kingdom*

(Manuscript received 20 July 1998, in final form 8 January 1999)

ABSTRACT

A simple model of the tropospheric circulation, based on a 10-level primitive equation model, is forced by linearly relaxing the potential temperature toward an idealized, zonally symmetric equilibrium field. The model equations are integrated in time until a statistically steady state is obtained. The local relationship between the state of the background flow, the direction of wave propagation, and subsequent wave breaking at the tropopause level is then investigated. Maps of potential vorticity (PV) on isentropic surfaces are analyzed and all four different types of wave breaking described recently by Peters and Waugh are shown to occur. It is found that cyclonic wave breaking events are usually initiated by poleward fluxes of wave activity, and anticyclonic events by equatorward fluxes. Composites are then used to show that equatorward fluxes are associated with a jet that is locally broad and weak, with relatively strong isentropic PV gradients to its equatorward flank. By contrast, poleward fluxes are associated with a narrow, strong jet, with very weak or even negative PV gradients on its equatorward side. It is argued that this result is consistent with nonlinear critical-layer theory, as under certain conditions an isolated region of homogenized potential vorticity must remain a perfect reflector of wave activity for all time.

The variability exhibited by the zonal flow field is then investigated using a cross-sectional EOF method. The first EOF is found to have similar structure in the latitude–height plane to the baroclinic waves themselves, and describes much of the variability associated with them. The second EOF has structure that corresponds to a sharp, narrow jet in its positive phase and a weak, broad jet in its negative phase. Its phase is shown to be well correlated with the wave activity flux index, with the maximum occurring at a space and time lag, with the phase of the EOF preceding the index. Most of the variability associated with this EOF occurs on the scale of zonal wavenumbers 2–4, suggesting that the direction of meridional propagation of the baroclinic waves is determined locally. Strikingly, the phase of the second EOF propagates in a wavelike manner, with wavenumber and period (≈ 11 –14 days) quite distinct from those of the baroclinic waves. Individual phase maxima of these long waves can persist for up to ≈ 20 –25 days, as they do not decay rapidly due to downstream radiation.

1. Introduction

In the last decade or so, much work has focused on the dynamics associated with Rossby wave breaking (e.g., McIntyre and Palmer 1984, 1985), greatly contributing to our understanding of transport in various atmospheric and oceanic flows. Recently, particular attention has been given to the breaking of synoptic-scale Rossby waves in the extratropical tropopause region. Such breaking has an important dynamical effect and leads to exchange of air between the troposphere and stratosphere. Wave breaking events have been analyzed in detail using observations of various tracer fields (e.g., Appenzeller and Davies 1992; Thorncroft et al. 1993, THM hereafter; Hartmann 1995; Appenzeller et al. 1996; Peters and Waugh 1996, PW hereafter). Direct

observational analysis has been supported by numerical simulations of tracer fields on isentropic surfaces using contour advection simulations driven by observed winds (e.g., Appenzeller et al. 1996; PW), which also give qualitative insight into the evolution of the finescale tracer fields during the breaking events. The observations and simulations have motivated the identification of four paradigms for tropopause wave breaking (PW, developing earlier ideas of THM). The four different paradigms may be summarized as follows.

- 1) In an anticyclonic “LC1-type” event, a tongue of stratospheric air extends upstream (i.e., westward) and equatorward and thins out as it is advected anticyclonically, often wrapping into small secondary vortices.
- 2) In an anticyclonic “P2-type” event, a broad extrusion of tropospheric air wraps itself up anticyclonically, forming a large cutoff “blocking” anticyclone. Peters and Waugh (1996) show that these events typically occur in regions of diffluent flow.
- 3) In a cyclonic “P1-type” event, which is a mirror image of (a) reflected about the jet axis, a tongue of

Corresponding author address: Dr. J. G. Esler, Centre for Atmospheric Science, Department of Applied Mathematics and Theoretical Physics, University of Cambridge, Silver Street, Cambridge, CB3 9EW, United Kingdom.
E-mail: j.g.esler@damtp.cam.ac.uk

tropospheric air extends upstream and poleward and thins out as it is advected cyclonically.

- 4) Similarly, in a cyclonic “LC2-type” event, which is a mirror image of (b), a downstream-tilting broad excursion of stratospheric air wraps up cyclonically, eventually forming a cutoff cyclone.

The desire to understand the dynamics of these wave breaking events has motivated numerous modeling studies. THM showed that the “basic” and “anomalous” baroclinic life cycle experiments of Simmons and Hoskins (1980) exhibited the characteristics of anticyclonic and cyclonic wave breaking, respectively. Once the waves in each life cycle reached maturity (days 6–9), the Eliassen–Palm (EP) cross section (Edmon et al. 1980) greatly differed between the two experiments. In the basic case the EP flux in the upper troposphere was directed strongly equatorward, indicating equatorward propagation of wave activity and leading to convergence in the subtropics. The wave activity was subsequently dissipated at low latitudes, as the waves broke. In the anomalous experiment the EP flux was directed poleward, and most of the wave activity was found to remain at high latitudes.

The two initial value experiments of THM differed only in that the initial flow in the anomalous case had additional cyclonic barotropic shear. Clearly, the background state must determine whether cyclonic or anticyclonic breaking takes place, but it is not clear if these experiments tell us anything of how changes in background state caused by internal tropospheric variability or nonzonality would affect wave breaking in a fully turbulent forced-dissipative flow. One important characteristic of such a flow is that the waves themselves tend to organize into coherent wave packets (e.g., Chang 1993; Lee and Held 1993), and the wave breaking may therefore be concentrated near the maxima of such packets.

Lee and Feldstein (1996) studied wave breaking in an aquaplanet GCM in which the circulation is driven by zonally symmetric forcing. Exploiting the link between EP-flux direction and the subsequent type of wave breaking discovered by THM, they established a relationship between the structure of the local linear quasigeostrophic refractive index and the direction of the local meridional component of the EP flux. Local values were defined by taking a local zonal average at the center of wave packets. Following Lee and Feldstein (1996) we shall refer to this as partial zonal averaging. They concluded that, when there was a large cavity in the midlatitudes in which linear wave propagation was possible, indicated by positive values of the refractive index field, then the flux was directed more poleward. When the cavity was smaller and the critical line for the waves was closer to the jet maximum, then the flux tended to be directed more equatorward.

Using a primitive equation model, Akahori and Yoden (1997) have recently considered a similar question: the effect of low-frequency variations in the zonal index (i.e., variations in the principal component of the leading EOF of the zonal mean wind) on the type of wave break-

ing event observed. To differentiate between anticyclonic breaking (on the equatorward side of the jet) and cyclonic breaking (on the poleward side of the jet), they defined a “life cycle index” to be the average latitude at which negative potential vorticity gradients are observed on a given isentropic surface. By correlating this life cycle index with the zonal index, they showed that when the jet was displaced poleward anticyclonic breaking was more common, and that cyclonic breaking was dominant when the jet moved equatorward.

The study described in this paper aims to go further by establishing a clear relationship between a diagnostic quantity—the local “background” zonal wind from which synoptic and smaller scales have been filtered—and the type of wave breaking event that is occurring locally. The results from a primitive equation model with zonally symmetric forcing are used. Using a cross-sectional EOFs method (see Esler 1997, appendix D), the model is shown to generate considerable internal variability, including coherent, propagating long waves that persist for up to ≈ 20 –25 model days. These are shown to have an important role in controlling wave breaking.

In section 2, the model and experiments are described. In section 3, we introduce a three-dimensional wave activity flux similar to that described in Esler and Haynes (1999) for the two-layer model, from which a flux index i is defined. The relationship between this index and the wave breaking events observed in the experiments is then quantified in section 4. In section 5, a composite method is used to determine the difference in the background flow between high and low index events. In section 6, these composites are compared with the leading cross-sectional EOFs of the background zonal flow, and it is shown that the phase of the coherent long waves mentioned above is well correlated with the flux index. Spatial and temporal lags in correlation are also calculated. In section 7, we discuss the sensitivity of the model runs to the boundary layer drag and radiative relaxation timescales, as well as the model resolution. Section 8 is a discussion of the results, principally with regard to nonlinear critical-layer theory, and in section 9 we state our conclusions.

2. The numerical model and methodology

The numerical model is designed to solve the primitive equations on a sphere in pressure coordinates given by

$$\frac{d\mathbf{u}}{dt} = -f\mathbf{k} \times \mathbf{u} - \nabla_H \Phi - \kappa_M \mathbf{u}, \quad (1)$$

$$\frac{d\Theta}{dt} = -r(\Theta - \Theta_E), \quad (2)$$

$$\frac{\partial \omega}{\partial p} + \nabla_H \cdot \mathbf{u} = 0, \quad (3)$$

and

$$\frac{\partial \Phi}{\partial \zeta} = -c_p \Theta, \quad (4)$$

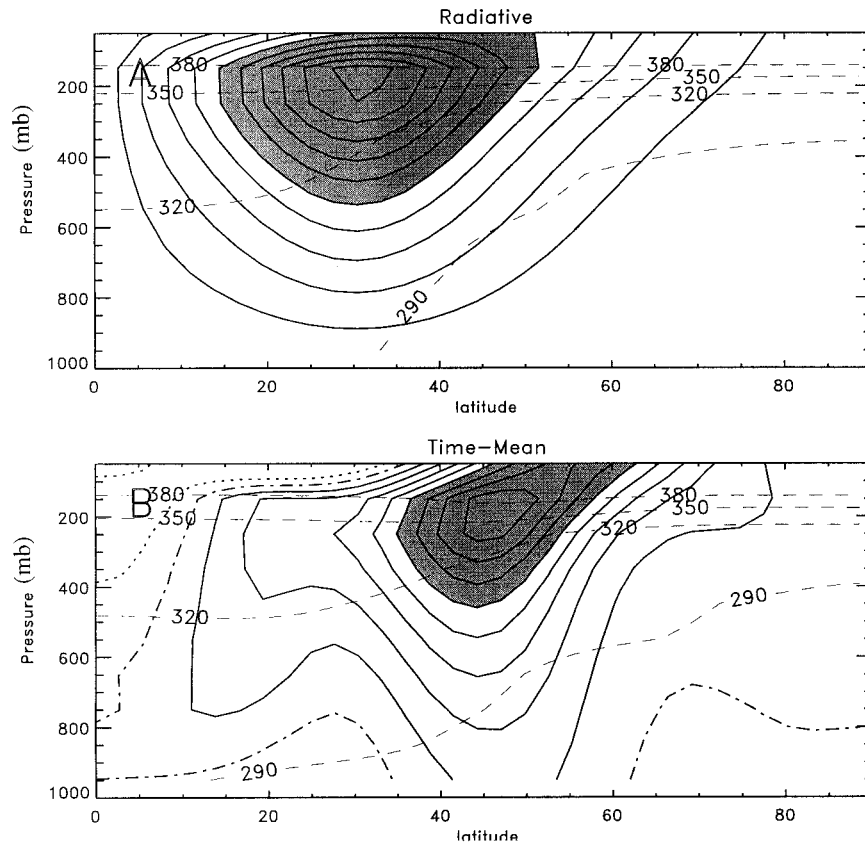


FIG. 1. (a) A contour plot of zonal wind \bar{u} corresponding to the radiative temperature field Θ_E . (b) A contour plot of the time-mean zonal wind \bar{u} . Contour intervals are 4 m s^{-1} , and values above 20 m s^{-1} are shaded. Negative values are contoured by dotted lines and the zero contour is dot-dashed. Superimposed on each plot are some labeled potential temperature contours (dashed) corresponding to the balanced temperature field.

where Φ is geopotential; ∇_H denotes the horizontal component of the gradient operator; $\zeta = (p/p_s)^\kappa$ an auxiliary vertical coordinate; Θ potential temperature; and Θ_E the equilibrium potential temperature field, to which Θ is relaxed on a timescale r^{-1} , which is set to 25 days. The model has mechanical damping on a timescale of κ_M^{-1} , which is nonzero only on the lowest pressure level, where its value is 0.5 days. This represents the effect of surface friction. Otherwise the notation is standard. The model has 10 equally spaced pressure levels, from 950 to 50 mb, and the pressure velocity ω is set to zero on the upper and lower boundaries. This is equivalent to setting the vertically integrated divergence to zero. This, in turn, implies a constraint on the vertical integral of geopotential, which imposes the value of geopotential at the lower boundary and allows the geopotential field to be calculated directly from the potential temperature field through (4). The horizontal discretization is spectral with T42 resolution. To prevent spurious build-up of enstrophy at grid scales, ∇^8 hyperdiffusion is included in (1) and (2). A timescale of 2 h on the smallest scale was found to be necessary to maintain numerical stability.

The model was allowed to “spin up” for a period of

600 days, and then the dynamical fields of four 100-day periods, each separated by 200 days, were analyzed in the Northern and Southern Hemispheres. Data were sampled from these 100-day periods once every day, except for one such period when they were sampled every 6 h.

The circulation is maintained by Newtonian relaxation applied to the potential temperature. The radiative equilibrium potential temperature field Θ_E is in thermal wind balance with a zonal jet of around 40 m s^{-1} . This potential temperature field and jet are shown in the upper panel of Fig. 1, and the time-mean potential temperature field and jet are shown in the lower panel. The structure of the radiative field was motivated by a desire to have some form of control over the location of the jet (partly for use in future experiments), and this choice, together with the uniformly long relaxation time, is the likely reason for a weaker-than-realistic Hadley cell circulation in the model. However, it is doubtful that any model with dry dynamics alone can hope to represent the Hadley circulation well, and as interaction between the Hadley circulation and Rossby wave breaking is not well understood (e.g., Held and Phillips 1990), we believe

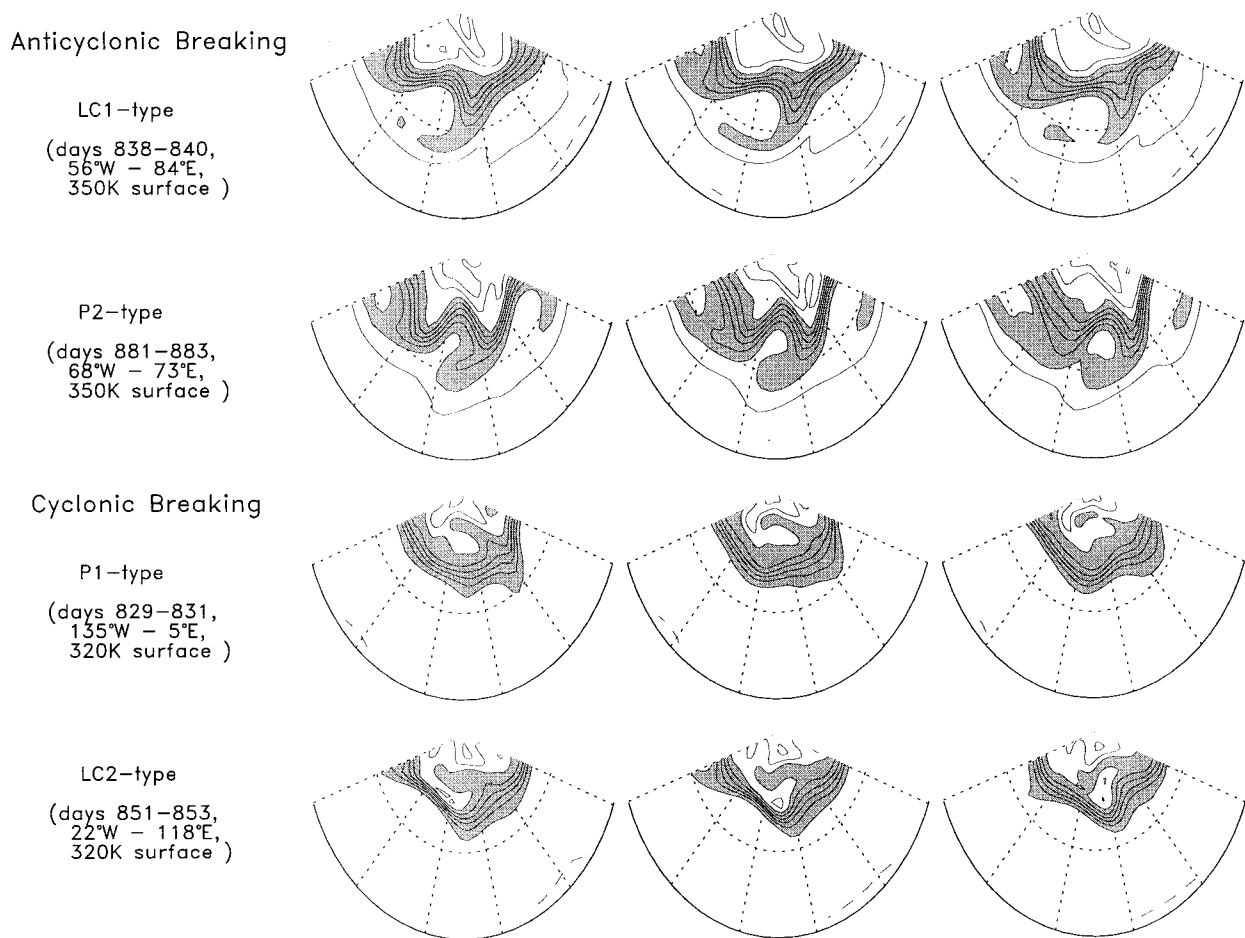


FIG. 2. Potential vorticity maps on isentropic surfaces illustrating different wave breaking events. Three consecutive days (left to right) are shown in each case. In the upper two cases, on the 350-K surface, the contour interval is 1.5 PVU with values between 3 and 10.5 PVU shaded ($1 \text{ PVU} = 10^{-6} \text{ m}^2 \text{ s}^{-1} \text{ K kg}^{-1}$). In the lower two cases, on the 320-K surface the contour interval is 1.1 PVU with values between 1.1 and 6.6 PVU shaded.

it merits an independent study. Apart from this, the tropospheric jets have similar magnitude and location compared with observations of Northern Hemisphere and Southern Hemisphere spring and autumn means (e.g., Hoskins et al. 1989). The most important difference, we believe, is that the region of strong latitudinal shear to the equatorward side of the jet is 5° – 10° poleward compared to observations. In the model there are also westerlies near the surface in the subtropics, although this is likely to be less significant for our experiments.

Figure 2 shows maps of potential vorticity (PV) on isentropic surfaces, illustrating that the four different types of wave breaking discussed in the introduction all take place in the model experiment. In these diagrams we have shaded a “tropopause region” of high PV gradient (defined as lying between two fixed values of PV) to help illustrate the events. The first two rows show three consecutive days during anticyclonic breaking events on the 350-K surface. Contours of PV- θ on the equatorward side of the jet are stretched upstream and equatorward, and then either are thinned out and dis-

sipated (in the LC1-type example) or are wrapped around and rejoin the tropopause region, forming a cutoff anticyclone (in the P2-type example). The other rows show the P1- and LC2-type events, which (as pointed out by PW) are simply mirror images of the LC1 and P2 events reflected about the jet axis. It was found to be much easier to illustrate these latter events on the 320-K surface, because on the 350-K surface the transition between the purely laminar region, with wavy contours, and the turbulent region, where the contour shapes are very irregular, was found to be very sharp on the poleward side of the jet. By contrast, on the 320-K surface this transition was found to be very sharp on the equatorward side of the jet.

Note that the LC2 and P2 events in the model are not as dramatic as those shown in the contour advection experiments of Appenzeller et al. (1996) and PW. In their experiments the cutoff anticyclones and cutoff cyclones formed during the breaking events deform the entire region of high PV gradient.

This difference is most likely due to the fact that,

because of the strength of the hyperdiffusion necessary to maintain numerical stability in our model (which is determined by the model resolution), the region of high PV gradient in the model is much broader in latitudinal extent than the tropopause region derived from observations, and is therefore much more prone to be partially eroded by wave breaking events than to be deformed across its entire width. It is also possible that the difference between our models time-mean state and the observed state is accountable. Peters and Waugh (1996) have also shown that P2-type events, which were relatively uncommon in our experiment, tend to occur in the strong diffluent regions present at the storm track exits. We do not force zonally localized storm tracks in our experiment, and this may partly explain the weak, infrequent nature of the P2-type events.

3. A wave-activity flux index

In order to diagnose wave propagation in the model, it is helpful to use a three-dimensional wave activity conservation relation of the form

$$\frac{\partial A}{\partial t} + \nabla \cdot \mathbf{F} = \mathcal{D}. \quad (5)$$

Plumb (1985) exploited the nonuniqueness in the derivation of the pseudomomentum flux to obtain a flux that had the group velocity property

$$\mathbf{F} = \mathbf{c}_g A \quad (6)$$

for small amplitude stationary waves in the WKB limit, without the need for phase averaging. Closely following Esler and Haynes (1999), where the same method is used for the two-layer model, we have used a correction related to Plumb's to generalize his result to nonstationary waves. Recently, Vanneste and Shepherd (1998) have shown that wave activity relations of this type always satisfy the group velocity property (6) provided that the coefficients of the linearized equations are slowly varying in space and time, a condition met by the WKB approximation that we are assuming here. In any case, it is easily shown explicitly that (6) holds in the WKB limit, following Plumb (1985).

The flux, which like that of Plumb (1985) is valid to $O(\alpha^2)$ in wave amplitude α , is then given by

$$\mathbf{F} = \frac{a \cos \phi}{2} \begin{pmatrix} \frac{2U^0 A}{a \cos \phi} + \frac{1}{2}(\psi^e q^e - v^e \xi^e) + v^{e2} - \frac{\psi^e v_\lambda^e}{a \cos \phi} \\ -u^e v^e + \frac{\psi^e u_\lambda^e}{a \cos \phi} \\ \frac{f}{\Theta_p^0} \left(v^e \theta^e - \frac{\psi^e \theta_\lambda^e}{a \cos \phi} \right) \end{pmatrix}, \quad (7)$$

and the wave activity by

$$A = a \frac{\cos \phi \left(q^{e2} - \frac{\xi^e q_\lambda^e}{a \cos \phi} \right)}{4Q_\phi^0}. \quad (8)$$

All quantities with a superscript (e.g., u^e) denote perturbation from a fixed basic state, which has zonal velocity U^0 , potential temperature Θ^0 , and quasigeostrophic potential vorticity Q^0 . These are generally taken to be the time-mean values. Here ψ^e is the perturbation streamfunction, the full streamfunction being given by $\Psi = \Phi/2\Omega \sin \phi$.

The perturbation quasigeostrophic potential vorticity is given in terms of ψ^e by

$$q^e = \frac{1}{a^2 \cos^2 \phi} \frac{\partial^2 \psi^e}{\partial \lambda^2} + \frac{1}{a^2 \cos \phi} \frac{\partial}{\partial \phi} \left(\cos \phi \frac{\partial \psi^e}{\partial \phi} \right) + f \frac{\partial}{\partial p} \left(\frac{\theta^e}{\Theta_p^0} \right). \quad (9)$$

The quantity ξ^e is defined by the expression

$$\xi_x^e = \frac{\xi_\lambda^e}{a \cos \phi} = q^e - \overline{q^e}. \quad (10)$$

(Overbars denote zonal means.) Uniqueness is imposed by the condition $\xi^e = 0$.

Figure 3 shows snapshots of meridional velocity and wave activity flux \mathbf{F} on the 350-mb level, on days 26 and 87 of the first 100-day period investigated. The contours on the wave activity plots show the convergence of the vertical component of the flux, $-F_p^{(p)}$, which can be thought of as a source of wave activity on that level. This source feeds the sinks of wave activity at low and high latitudes, where wave breaking and dissipation tend to occur. Note that the eddies in the meridional wind field snapshots are clearly organized into groups or packets (see, e.g., Chang 1993; Lee and Held 1993). On day 26, from 175°E eastward to 20°W, there is an example of a long baroclinic wave packet that is chiefly undergoing equatorward radiation of wave activity, particularly at its downstream end. Notice the strong northeast–southwest tilting of the eddies in the meridional wind field in this region, which is characteristic of this type of behavior. By way of contrast, at day 87, from 100°E eastward to 90°W, there is an example of a packet undergoing strong poleward radiation at its upstream end. This poleward radiation is marked by a northwest–southeast tilting of the eddies in this region (seen in the meridional velocity contours, e.g.).

In both snapshots there is also a distinct wavelike pattern visible in the wave activity flux fields, with the waves propagating alternately poleward and equatorward as one moves in longitude. The length scale of these variations in meridional flux is clearly distinct from the length scale associated with the eddies (waves 2–3 as opposed to waves 6–7). We shall go on to show

that they are related to coherent structures in the background flow.

A useful diagnostic of the upper-tropospheric behavior of the waves locally is given by the meridional component of this flux $F^{(\phi)}$. This is investigated over a region 20° – 80° N and an index of flux direction is defined as follows:

$$i(\lambda, t) = \frac{\left\langle \int_{\phi,p} F_-^{(\phi)} \right\rangle \int_{\phi,p} F_+^{(\phi)} - \left\langle \int_{\phi,p} F_+^{(\phi)} \right\rangle \int_{\phi,p} F_-^{(\phi)}}{\left\langle \int_{\phi,p} F_+^{(\phi)} \right\rangle \left\langle \int_{\phi,p} F_-^{(\phi)} \right\rangle}, \quad (11)$$

where

$$F_+^{(\phi)} = \begin{cases} F^{(\phi)} & \text{if } F^{(\phi)} > 0 \\ 0 & \text{otherwise,} \end{cases} \quad (12)$$

$$F_-^{(\phi)} = \begin{cases} -F^{(\phi)} & \text{if } F^{(\phi)} < 0 \\ 0 & \text{otherwise.} \end{cases}$$

Brackets $\langle \rangle$ indicate averaging over λ and t , and the symbol $\int_{\phi,p}$ is used to denote

$$\int_{\phi,p} = \int_{p_0}^0 \int_{20^\circ}^{80^\circ} \cos\phi \, d\phi \, dp.$$

Here i is further normalized by dividing by $\sqrt{\langle i^2 \rangle}$.

The index i has been constructed to have the following desirable properties.

- 1) The index i is negative (in the Northern Hemisphere) if the meridional component of the flux, $F^{(\phi)}$, is directed entirely equatorward and positive if it is entirely poleward.
- 2) The average $\langle i \rangle = 0$ so that it is a suitable variable to use in the correlation analysis that follows.
- 3) The index i is proportional to the magnitude of $F^{(\phi)}$ in the sense that if $F^{(\phi)}$ is doubled at every latitude and height at some position (λ_0, t_0) , then i will be doubled at that position (ignoring any slight correction to the normalization constant). Note that multiplying $F^{(\phi)}$ by -1 at (λ_0, t_0) does not cause $i \rightarrow -i$. If there is little wave activity, then $i \approx 0$. However, $i \approx 0$ does not necessarily imply the absence of wave activity, although in practice this is usually the case.

Condition 3 is necessary because otherwise regions of very low wave activity would have equal weighting in the correlation analysis that follows to those regions where the baroclinic waves had their greatest amplitude. Equation (11) is possibly the simplest formulation that meets these three conditions.

The ratio given by

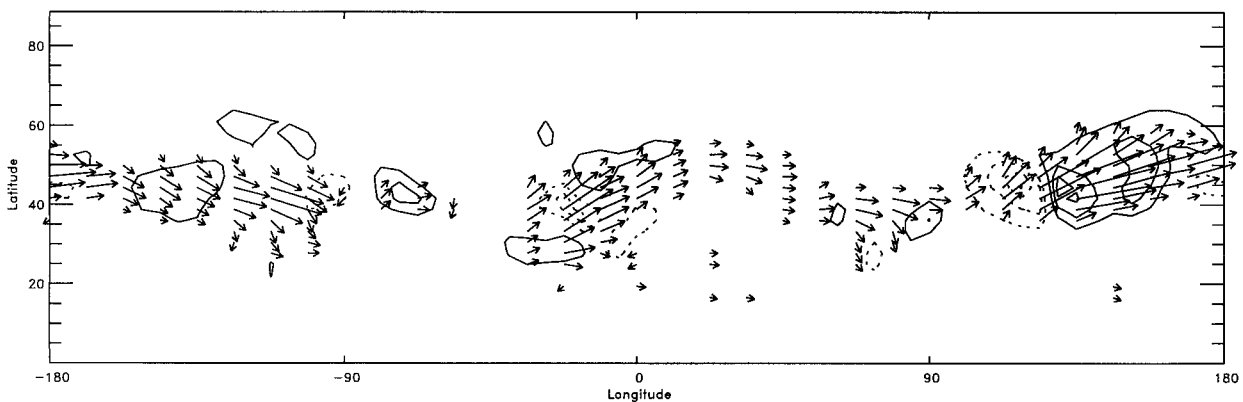
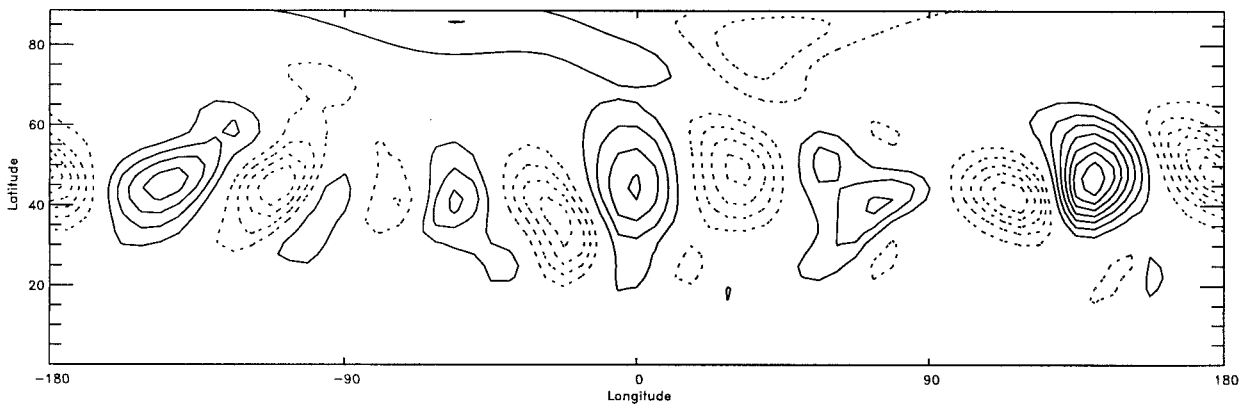
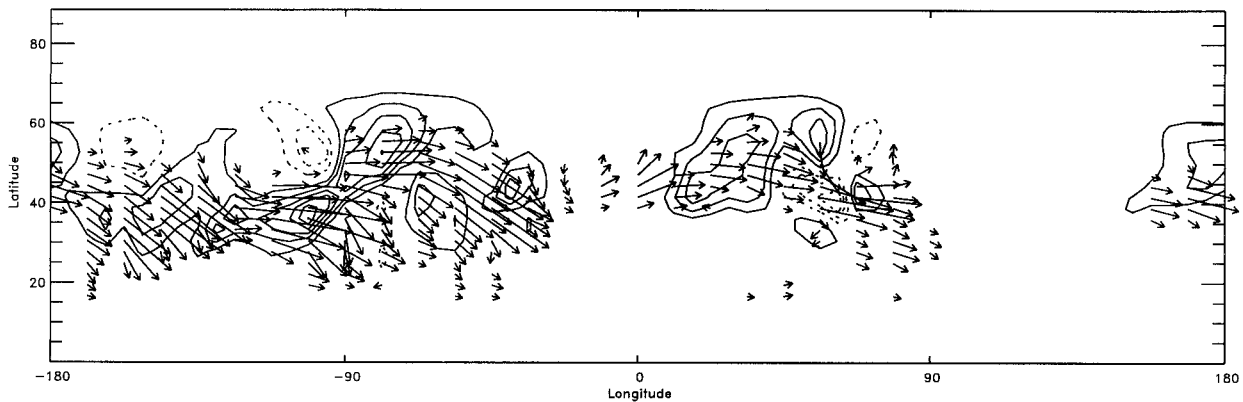
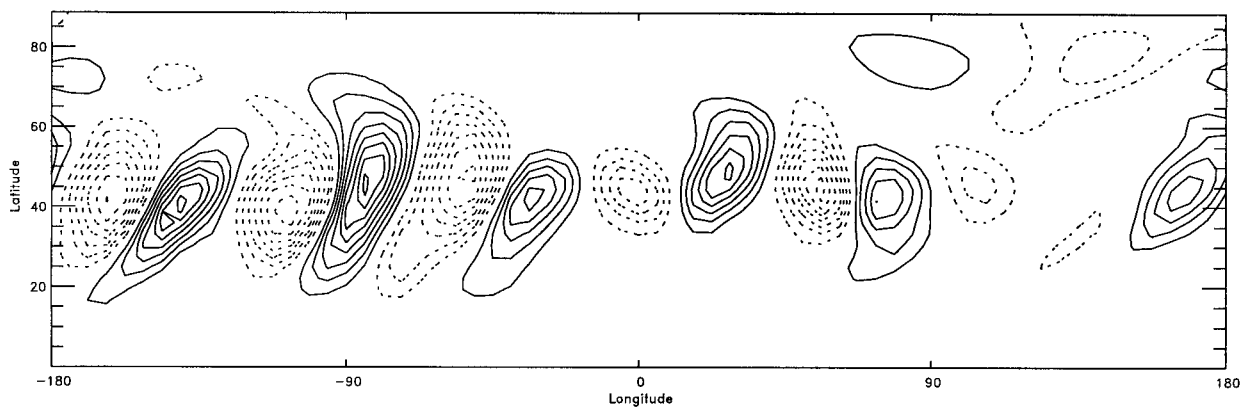
$$\frac{\left\langle \int_{\phi,p} F_+^{(\phi)} \right\rangle}{\left\langle \int_{\phi,p} F_-^{(\phi)} \right\rangle}$$

had a value between 0.36 and 0.45 for each 100-day period analyzed. This means that i becomes positive (in the Northern Hemisphere) if and only if the poleward flux in a latitude–pressure cross section exceeds around 40% of the equatorward flux. Regions in (λ, t) space where $i > 0$ are termed poleward radiating (PR) regions, and regions where $i < 0$ are termed equatorward radiating (ER) regions. Figures 4a and 4b, respectively, show composite meridional–height cross sections, showing $(\cos\phi)(F^{(\phi)}, F^{(p)})$, averaged over those regions in the (λ, t) plane where (a) $i > 1$ and (b) $i < 1$. [Between 10% and 15% of all the (λ, t) points in each 100-day period fall into each category.] These are therefore examples of “typical” poleward- and equatorward-radiating regions. Figures 4c and 4d then show meridional cross sections of the flux for a strongly poleward-radiating region and a strongly equatorward-radiating region on days 27 and 88 at 47° W and 147° E, respectively (this can be compared with Fig. 3, which shows the previous days).

4. The relationship between wave breaking and the flux index

It has been shown by several authors (e.g., THM; Magnusdottir and Haynes 1996) that in idealized life cycle experiments, that is, initial value problems, equatorward fluxes of wave activity are associated with anticyclonic (more specifically LC1 type) wave breaking events, and poleward fluxes with cyclonic (LC2 type) events. However, it is an open question whether a similar result holds for a forced-dissipative experiment such as ours in which wave breaking is an ongoing process occurring at isolated longitudes and times. To this end we attempted to record $i(\lambda, t)$, as defined in section 3, at the locations of wave breaking events to determine what kind of relationship exists.

An initial investigation soon revealed that a strong correlation would exist only at locations associated with the initiation of a wave breaking event, very early in its development. To identify such locations, it is helpful to use the following definition: A PV- θ contour is defined to be “overturning” if a line drawn from pole to equator at a given longitude crosses it more than once. For example, the contour shown in Fig. 5a is overturning between the two dotted lines. PV- θ contours can be chosen close to the jet center (on its equatorward flank if we are interested in anticyclonic events, or its poleward flank for cyclonic events) that become overturning only occasionally, and in regions that are reasonably confined in longitude. Unsurprisingly, examination of PV- θ maps shows that when such a contour becomes



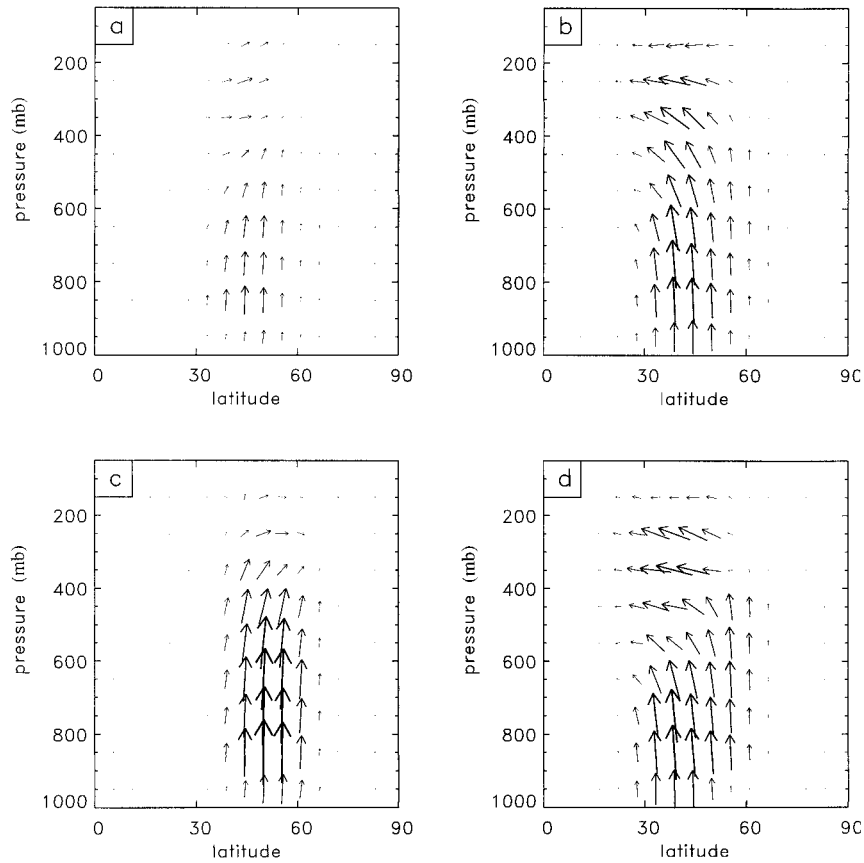


FIG. 4. Flux cross sections showing $(\cos\phi)(F^{(\phi)}, F^{(p)})$ in the meridional height plane: (a) a composite showing the mean structure of $(\cos\phi)(F^{(\phi)}, F^{(p)})$ for those points (λ, t) where $i > 1$; (b) As in (a) but for $i < 1$; (c) an extreme example of poleward radiation (day 88, 147°E , $i = 5.56$); (d) an extreme example of equatorward radiation (day 27, 47°W , $i = -4.18$). Arrow scales are (a), (b) 10° to $250a \text{ m}^2 \text{ s}^{-2}$, where a is the earth's radius, and 100 mb to $2.5 \times 10^7 \text{ kg m s}^{-4}$; and (c), (d) 10° to $500a \text{ m}^2 \text{ s}^{-2}$, and 100 mb to $5 \times 10^7 \text{ kg m s}^{-4}$.

overturning it almost invariably precedes a large wave breaking event that takes place farther from the jet center over the following 1–2 days.

Two 100-day periods were analyzed to identify the locations and times of the initiation events, the locations being taken to be the easternmost grid point of any overturning region, using the preceding definition of overturning. In Fig. 5a, points A and B are located on the easternmost longitudinal gridpoint of the overturning region. Point C is on the neighboring grid point to the east. In the numerical algorithm used for the identification of the initiation events, the additional condition that the latitude of point C must be closer to the latitude of point B than that of point A was imposed. This was to prevent the inclusion of longitudes asso-

ciated with occasional cutoff vortices. (The reader should note that this algorithm works perfectly in the limit of infinitely many longitudinal grid points.)

The results of the analysis are shown in Fig. 5b. Four contours were chosen: two on the equatorward side of the jet on the 350-K surface, the 4.75- and the 5.25-PVU (PV units) contours, to investigate anticyclonic events; and two on the poleward side of the jet on the 320-K surface, the 4.9- and 5.4-PVU contours, to investigate cyclonic events. The 4.75-PVU–350-K contour was found to be overturning in 67 locations over the 2×100 days and the distribution of i at these locations is shown in the upper left panel. Superimposed is a curve showing the (approximately normal) distribution of i over all longitudes and times. It shows that anticyclonic breaking

←

FIG. 3. Snapshots of meridional velocity and the horizontal components of the wave activity flux on days 26 and 87, at the 350-mb level. Contours on the wave activity picture show the magnitude of the convergence of the vertical component of the flux $-F_p^{(p)}$. Contour intervals are 5 m s^{-1} and $500 \text{ m}^2 \text{ s}^{-2}$, respectively. Arrow scales are 1° to $25a \text{ m}^2 \text{ s}^{-2}$, where a is the earth's radius. Solid contours denote positive values and dashed contours negative values.

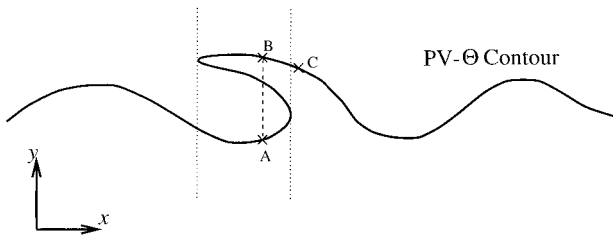


FIG. 5. (a) A schematic picture illustrating where the location of the initiation of a wave breaking event is defined to be (see text for details).

events are clearly associated with negative values of i (statistical significance at the 99.9% level is easily demonstrated using a Student's t -test for all four examples shown). Similar results are obtained for the 5.25-PVU-350-K contour, which is closer to the jet center and is overturning less frequently (in 27 locations). Comparable results are obtained for the 5.4-PVU-320-K and 4.9-PVU-320-K contours, showing that positive values of i are the norm at the initiation of cyclonic events.

There did not appear to be any simple relationship between i and whether a given anticyclonic event evolved into an LC1- or P2-type event, or similarly whether cyclonic breaking evolved into an LC2- or P1-type event. This must depend on both the details of the background flow and the geometry of the waves; for example, PW showed that P2 events often occurred in

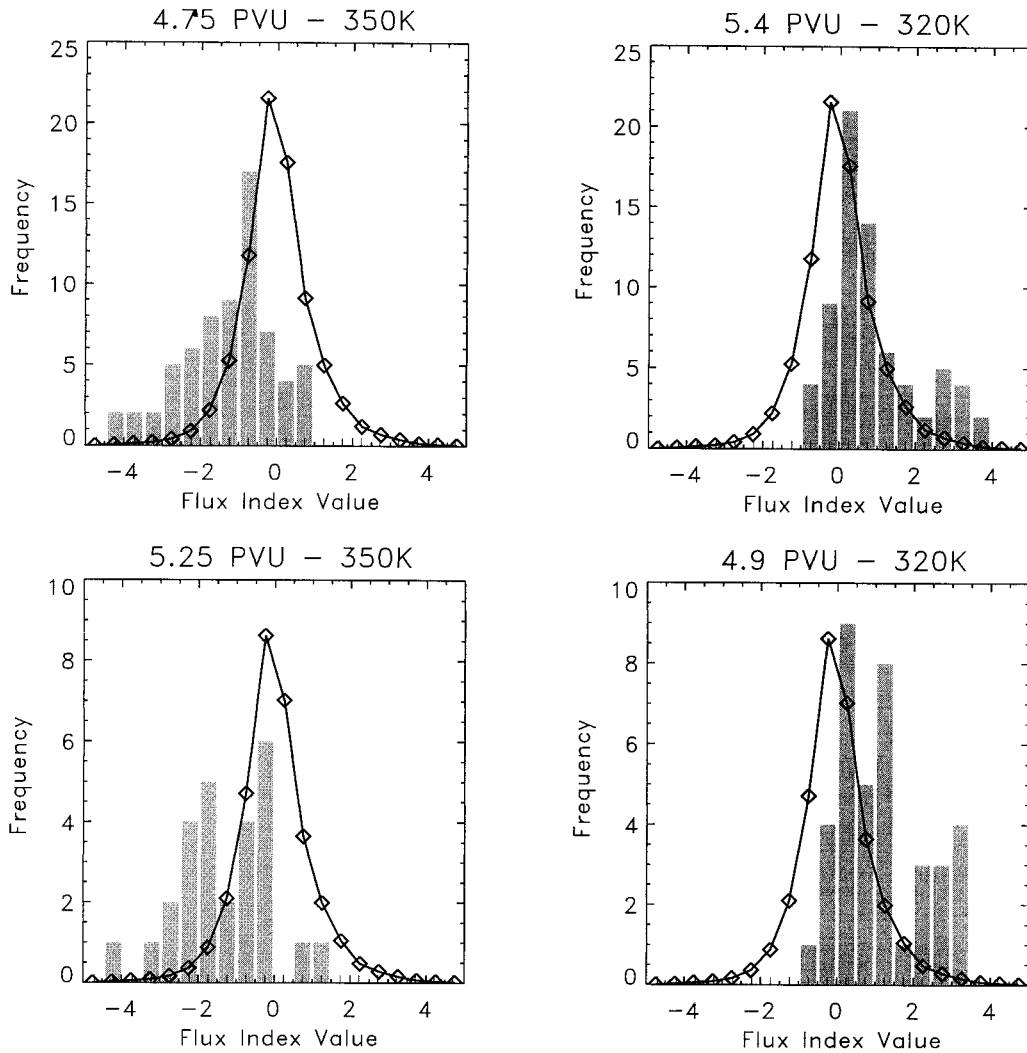


FIG. 5. (b) Bar charts illustrating the distribution of the value of the flux index i measured at the location of the initiation of wave breaking events over two 100-day periods of the integration. The two left-hand pictures refer to the initiation of anticyclonic breaking events on the 350-K surface, defined with reference to the 4.75- and 5.25-PVU contours, respectively. The two right-hand pictures refer to the initiation of cyclonic breaking events on the 320-K surface, identified using the 5.4- and 4.9-PVU contours. The solid curve superimposed on each bar chart shows the distribution of i at all locations.

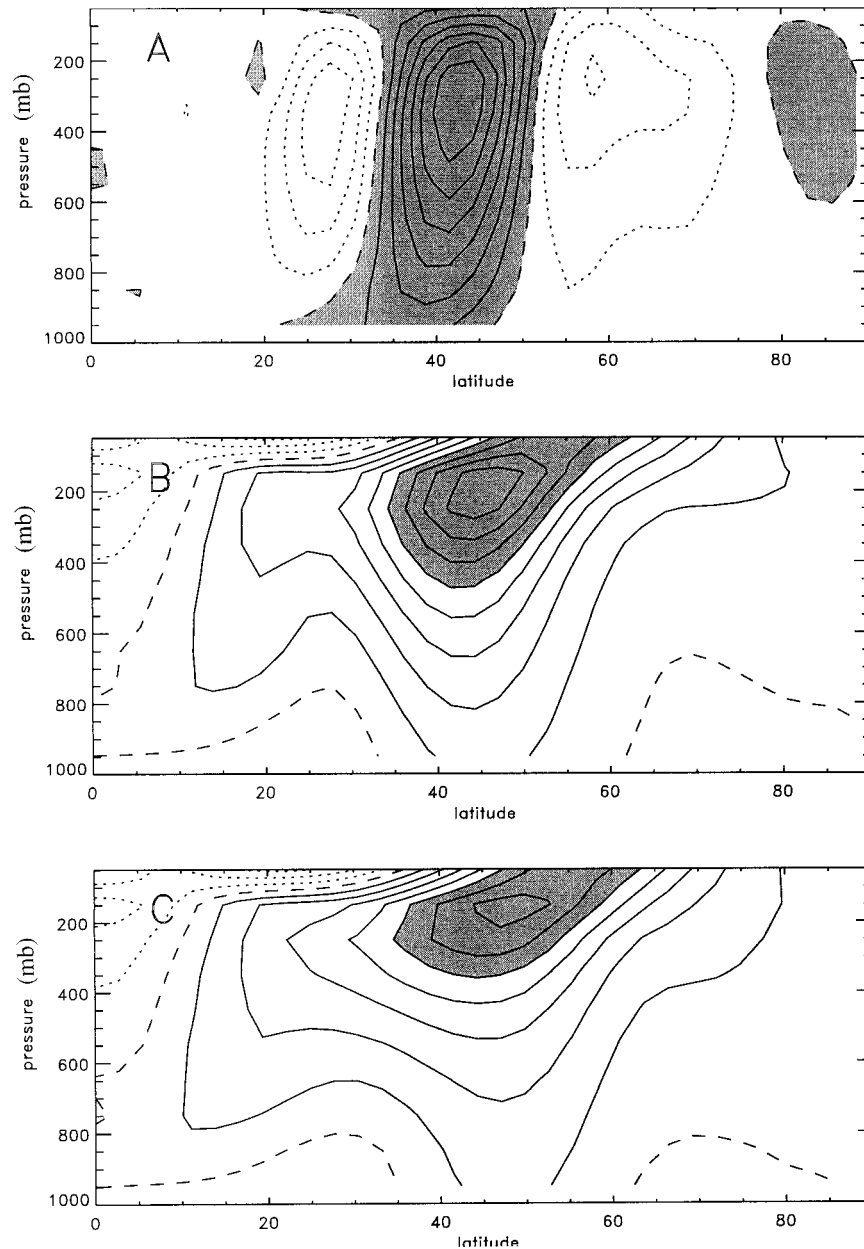


FIG. 6. (a) A composite zonal wind picture for the first 100-day period. Background zonal wind fields for regions with $i < -1.0$ (ER) are subtracted from background zonal wind fields for regions with $i > 1.0$ (PR). The contour interval is 1 m s^{-1} ; positive values are shaded. (b) The composite background zonal wind for the PR regions ($i > 1$). (c) The composite background zonal wind for the ER regions ($i < -1$). The conventions used in plotting (b) and (c) are as for Fig. 1, i.e., a 4 m s^{-1} contour interval.

regions of diffluent flow, and this topic clearly merits further study. Because of these results, we shall differentiate only between anticyclonic and cyclonic events in the remainder of this paper.

5. Composites of the background flow

One simple method to determine the relationship between the background flow and the direction of the wave

propagation is to take composites. The background zonal wind, defined as the zonal mean and first five wave-numbers only, is averaged at all those (λ, t) points with $i > 1$, and then at all those points with $i < -1$. The difference between the background zonal wind between the $i > 1$ and $i < -1$ composites is shown in Fig. 6a, and the composites themselves in Figs. 6b and 6c, respectively. These figures show that PR regions ($i > 1$) are associated with a sharp strong jet, with a maximum

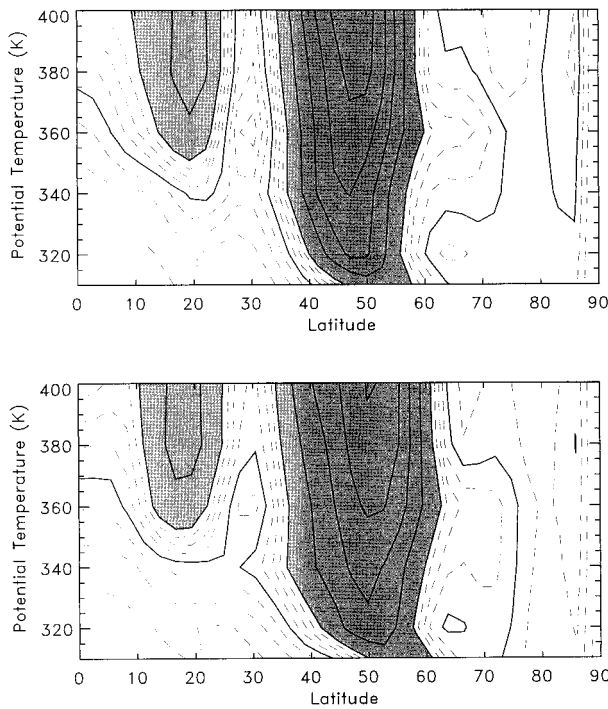


FIG. 7. Composites of PV gradient measured on isentropic surfaces from 310 to 400 K. (upper) PR regions ($i > 1$); (lower) ER regions ($i < -1$). Contour intervals are $10 \text{ PVU } a^{-1}$ (where a is the earth's radius) for the solid contours, with values above $20 \text{ PVU } a^{-1}$ shaded (so that the isolated solid contour represents $10 \text{ PVU } a^{-1}$). Also included are dashed contours with interval $2.5 \text{ PVU } a^{-1}$ up to the value of $20 \text{ PVU } a^{-1}$ to show more clearly the regions of weak PV gradient.

at around 45°N , and that ER regions ($i < -1$) are associated with a much broader weaker jet with its maximum displaced around 2° – 3° poleward. Nearly identical pictures were obtained for each hemisphere for all four 100-day periods, the maximum amplitude of the difference in the composites varying by less than 20%. Notably, Fig. 6a is very similar in structure to the correction to the zonal mean winds calculated by Akahori and Yoden (1997) as more likely to result in cyclonic than anticyclonic breaking.

The same method is then applied to the meridional gradient in background potential vorticity calculated on isentropic surfaces from 310 to 400 K. Figure 7 shows the composites for the PR (upper panel) and ER (lower panel) regions. There are two striking things about these pictures. First, there is the very strong PV gradient around 50°N that presumably acts as a waveguide (e.g., Swanson et al. 1997). Second, there is a region of very weak PV gradient at around 30°N , the region where the waves break to the equatorward side of the jet. The main differences between the two panels is that in the PR case there is a much stronger PV gradient in the extratropics and a much smaller minimum (by a factor of 4) in the PV gradient equatorward of this. A composite with $i > 1.5$ (not shown) shows a small region of neg-

ative PV gradient in this area. Poleward of the region of maximum gradient, the PR case has stronger PV gradient at upper levels, above 340 K, and lower PV gradient below this level.

6. A cross-sectional EOFs study

Another method, perhaps more comprehensive, that can be used to investigate the relationship between the background flow and the flux index is the cross-sectional EOFs method described in Esler (1997, appendix D).¹ This method can be used to decompose the full zonal flow into structures in the latitude–height plane, each of which explain optimal amounts of the variance of the flow in longitude and time. The first two EOFs calculated using this method are shown in Fig. 8 and describe 34.04% and 24.25% of the variance in the untruncated zonal wind field u , respectively. The remaining EOFs each explained less than 10% of the variance. The positive phase of the first EOF implies a local deviation of the zonal jet equatorward, and its negative phase a poleward deviation. Since such deviations in the position of the zonal jet are associated with the phases of baroclinic waves themselves, it is therefore natural to associate this EOF with those waves. Figure 9 shows the evolution in longitude and time of the perturbation meridional wind v' at 250 mb, averaged between 30° and 60°N , as well as the evolution of the principal components of the first two EOFs. In the v' picture (Fig. 9a) it is clear that the waves are organized into wave packets with amplitudes, phase speed, and group speed comparable with Southern Hemisphere observations (cf. Lee and Held 1993, Fig. 2). The first EOF principal component picture (Fig. 9b) shows that this EOF has captured a great deal of the variance of the u field associated with these packets. The progress of a given wave packet can be traced in either Fig. 9a or 9b, the signal in the u field leading the signal in the v' field by $\pi/2$ in phase. Note that there is a great deal more variability on longer length scales (i.e., waves 1–3) in the EOF1 picture compared with the v' picture. This can be explained by the fact that the meridional velocity is a longitudinally “differentiated” quantity compared with zonal velocity, and contains more variability at higher longitudinal wavenumbers.

The structure of the second EOF shown in Fig. 8b is very similar to the difference between the zonal flow composites taken in the PR and ER regions (Fig. 6a). We might, therefore, expect the phase of this EOF to be well correlated with the flux index, and therefore to influence the type of wave breaking events that subsequently occur. Of considerable interest then is the type of variability that this EOF exhibits. This is shown in Fig. 9c. The variability is clearly wavelike, with long waves (wavenumbers 2–4) propagating eastward at an

¹ The method described in Esler (1997) is for the two-layer model but is easily adapted for this multilevel case.

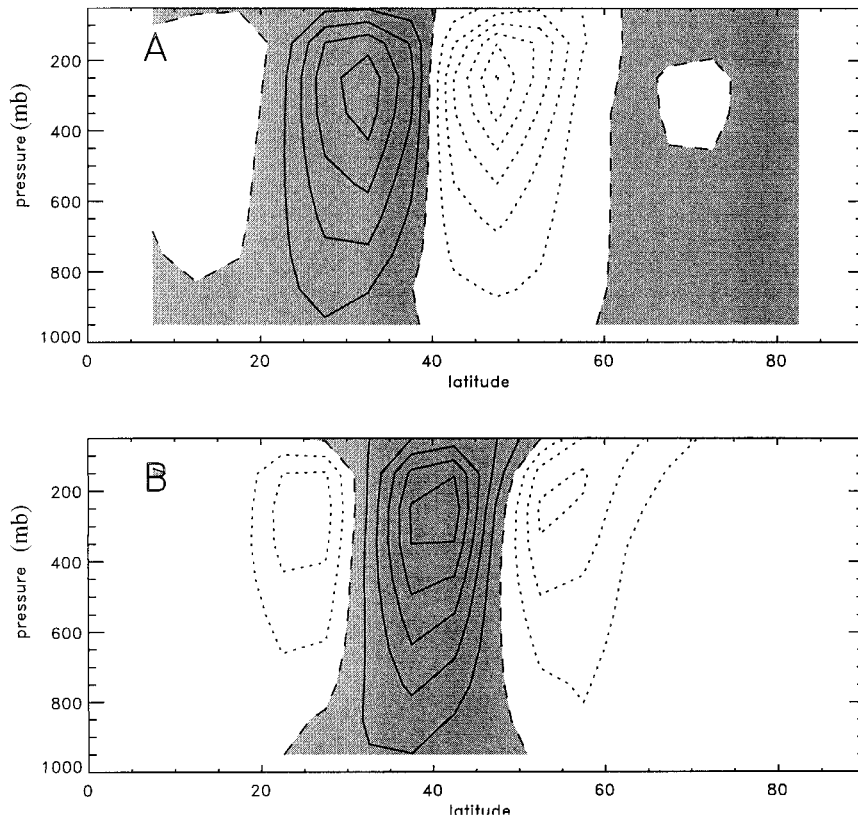


FIG. 8. The leading two cross-sectional EOFs from the first 100-day model period. Contour intervals are arbitrary (but taken to be 1 m s^{-1} for use with the evolution picture; Fig. 9) and positive values are shaded.

angular phase speed ($\approx 0.1 \text{ days}^{-1}$) that appears to be slightly faster than the phase speed of the baroclinic waves ($\approx 0.085 \text{ day}^{-1}$), but is much slower than their group velocity ($\approx 0.6 \text{ day}^{-1}$).²

The difference in wavenumber, and the fact that these waves can persist for up to ≈ 20 – 25 model days, shows that we are looking at independently propagating structures, rather than just a different projection onto the variability of the baroclinic waves themselves.³ Figure 10 shows a contour plot of the autocorrelations of the principal components of EOF1 and EOF2 with lag in longitude along the x axis and time lag along the y axis. These autocorrelations illustrate the main features of the variability associated with each EOF described above.

² This means that the waves are not forced directly by the envelope of the wave packets, although the phase of the long waves is not *entirely* independent of packet position. See, for example, the composites shown in Esler and Haynes (1999, Figs. 19 and 20) taken at the maxima of wave packets in this model experiment.

³ If the EOFs method is applied directly to the background zonal wind (as defined in section 5), as opposed to the full zonal wind field, the leading EOF has the structure of EOF2 and describes 31.86% of the variance. The second EOF has the structure of EOF1 and describes apparently random variability at large length scales.

Figure 11 shows a contour plot of the space- and time-lagged correlations between the flux index i and the principal components of EOF2. The lagged correlation field $c_{ab}(\lambda_{\text{lag}}, t_{\text{lag}})$ between two fields $a(\lambda, t)$ and $b(\lambda, t)$ is given by the equation

$$c_{ab}(\lambda_{\text{lag}}, t_{\text{lag}}) = \frac{\langle a(\lambda - \lambda_{\text{lag}}, t - t_{\text{lag}})b(\lambda, t) \rangle}{\sqrt{\langle a(\lambda - \lambda_{\text{lag}}, t - t_{\text{lag}})^2 \rangle} \sqrt{\langle b(\lambda, t)^2 \rangle}}, \quad (13)$$

where $\langle \rangle$ denotes averaging over all λ and t . [The dataset with 6-hourly data was chosen for this diagram, and the correlations plotted are in fact an average between the Northern Hemisphere and (minus the) Southern Hemisphere results.] This figure confirms the impression gained from the composite analysis, that there is a strong positive correlation (in the Northern Hemisphere) between the EOF phase and the flux index. In interpreting the magnitude of this correlation one should remember that the flux index i is small where the wave amplitude is small, but the projection of the zonal flow onto EOF2 is at most only weakly correlated with wave amplitude. This means that regions where the wave amplitude is small do not contribute to the total correlation, and that the relationship between i and the EOF phase in regions

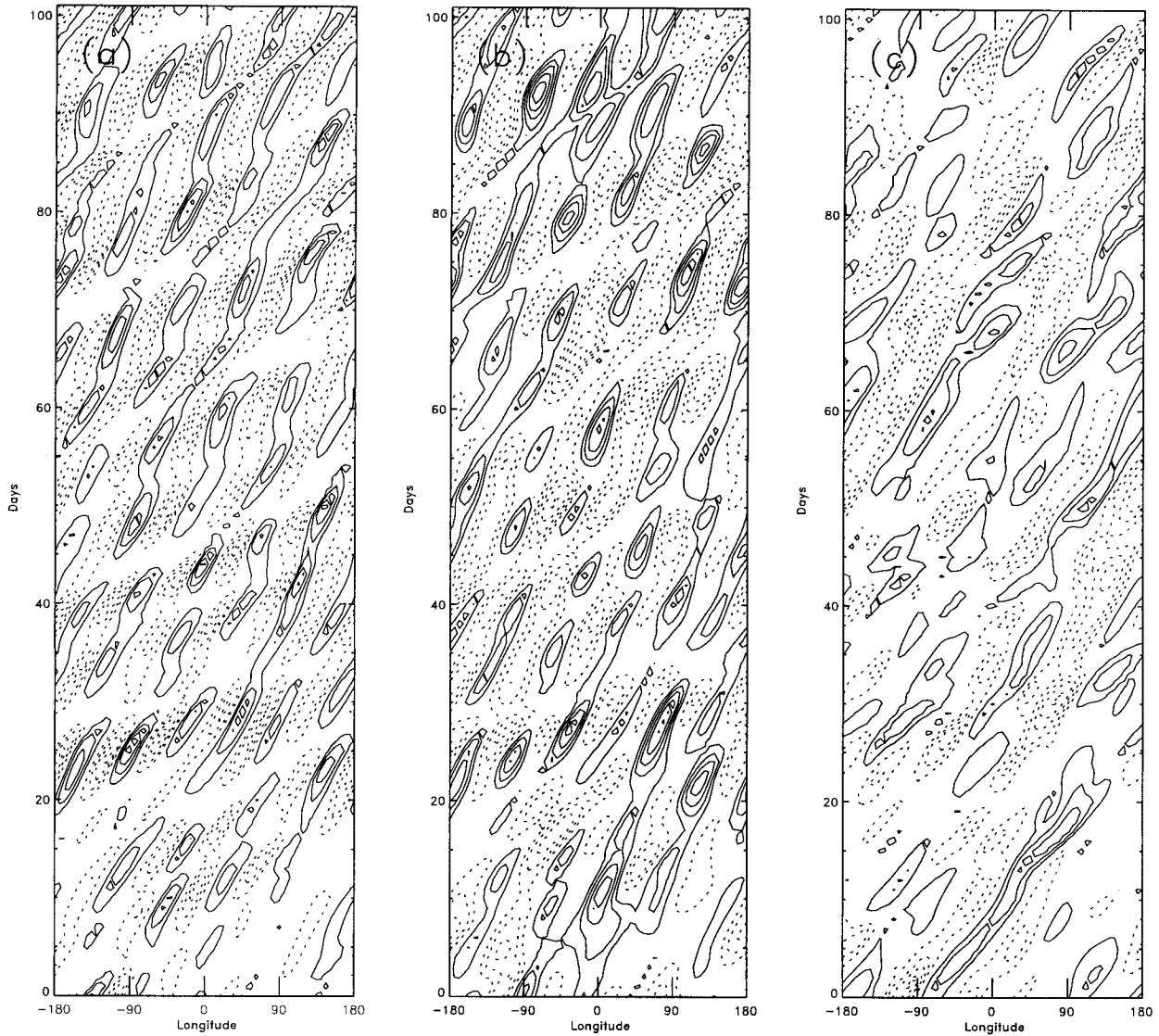


FIG. 9. Longitude–time plots showing the evolution of (a) perturbation meridional wind v^e at 250 mb, integrated in latitude from 30° to 60°N , (b) the principal components of EOF1, and (c) the principal components of EOF2. Contour intervals are (a) 6 m s^{-1} , and (b), (c) 1.0.

where the wave amplitude is large is therefore stronger than indicated by the correlation coefficient.

The maximum correlation in Fig. 11 occurs at a significant time and space lag, of about 12 h and 10° . The sense of this lag is such that the EOF phase precedes the maximum response in i , which occurs downstream. There is a velocity associated with the space lag and time lag, illustrated by the gradient of the arrow in Fig. 11, that is of the order of the wave packet group velocity.

Table 1 shows the Northern and Southern hemisphere results for the other periods studied (note that i is opposite in sign in the Southern Hemisphere). There is some variance in the magnitude of the correlation, although poor correlations may be partly explained by the fact that the EOF method works less well when the

position of the zonal mean jet varies greatly over the 100-day period. (The composite method is less sensitive to this, and perhaps as a result there is less variance in those results.) However, the correlation is reproduced in every period investigated, and in nearly every case the maximum occurs at a similar space and time lag. (Here it should be borne in mind that the data is sampled only once daily except for those datasets marked with an asterisk.)

7. Sensitivity to model parameters

Table 2 shows the results from a sensitivity study in which some of the parameters controlling the flow statistics have been varied. The sensitivity of the long

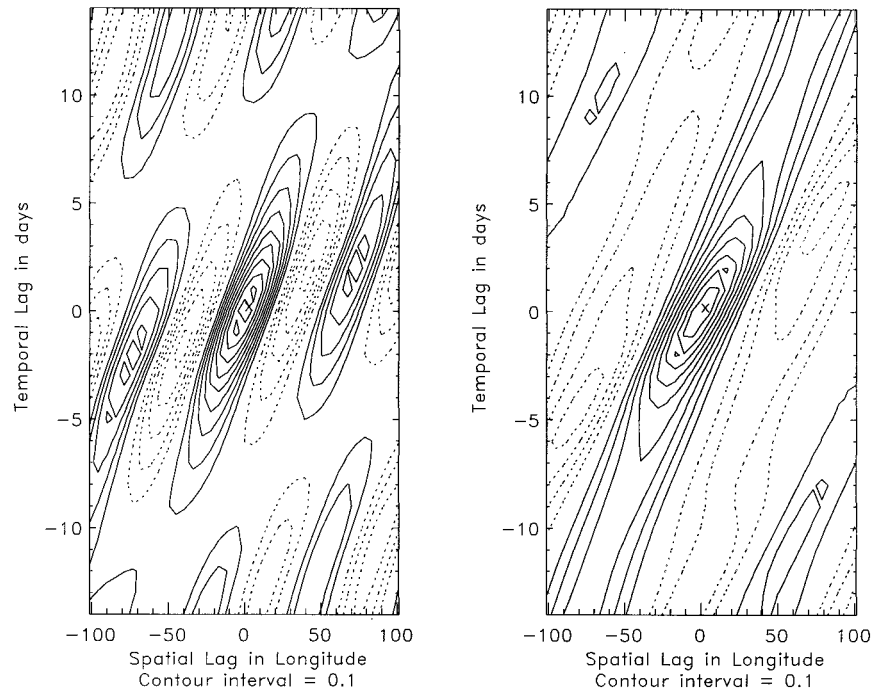


FIG. 10. Autocorrelations of the principal components (plotted in Fig. 9) of the leading two cross-sectional EOFs shown in Fig. 8. The contour interval is 0.1, negative contours are dashed, and positive contours are solid. The zero contour is omitted.

waves described in section 6 to these parameters is of particular interest here. In Table 2 the standard run described in sections 2–6 is marked †. Increasing the surface friction coefficient κ_M or the radiative relaxation r was found to move the time-mean jet equatorward, and decreasing the radiative relaxation was found to move it poleward. PV- θ plots (not shown) suggest that the result of Akahori and Yoden (1997), namely, that wave breaking is on average directed more equatorward when the jet moves poleward, and more poleward when the jet moves equatorward, also applies here. In particular, there is noticeably more poleward breaking in the $r^{-1} = 15$ days experiment compared with the $r^{-1} = 50$ days experiment, and more equatorward breaking in the $r^{-1} = 50$ days case. In every experiment the first two EOFs of u have near identical structure to those in Fig. 8, except that they tend to be centered close to the jet maximum in each case. From Table 2 the long waves, described by EOF2, are clearly damped by increased radiative relaxation, and to a lesser extent by increased surface friction. However, their period and wavenumber were not found to be greatly affected by changing r or κ_M . The run marked ‡ is a low-resolution (T21) experiment. The long waves found in the T42 experiments were also observed here and had similar structure in the meridional plane. However, they had a shorter wavelength (waves 4–5) and persisted for shorter periods compared with the T42 case.

As a further check on the reproducibility of these results, particularly at high resolution, the methods used

to produce the composite zonal flow diagram (Fig. 6) were applied to the results from an experiment using another simple general circulation model. These experiments will be reported in more detail in a forthcoming paper by Haynes and Scinocca. Briefly, however, the model is formulated in sigma coordinates and was run at high horizontal resolution (T85) and vertical resolution (31 levels). The temperature field was relaxed toward an equilibrium profile that was balanced with a zonal flow that was in solid body rotation on each level, and had constant shear in the vertical. Despite all these differences, the difference in the composite background zonal wind (not shown) between poleward- and equatorward-radiating regions, was very similar to that shown in Fig. 6. It had a positive maximum of magnitude $\approx 5 \text{ m s}^{-1}$ just equatorward of the jet core, and weaker negative minima to each side, illustrating the model independence of these results.

8. Discussion

To what extent may the theory of linear wave propagation, combined with nonlinear critical-layer theory, be applied toward understanding the relationship we have discovered between the flux index and the background flow fields, particularly the PV gradient (Fig. 7)? THM discussed this question in the slightly simpler context of their two wave-6 baroclinic life cycle paradigms (for LC1-type anticyclonic wave breaking and LC2-type cyclonic breaking). First, they used nonlinear

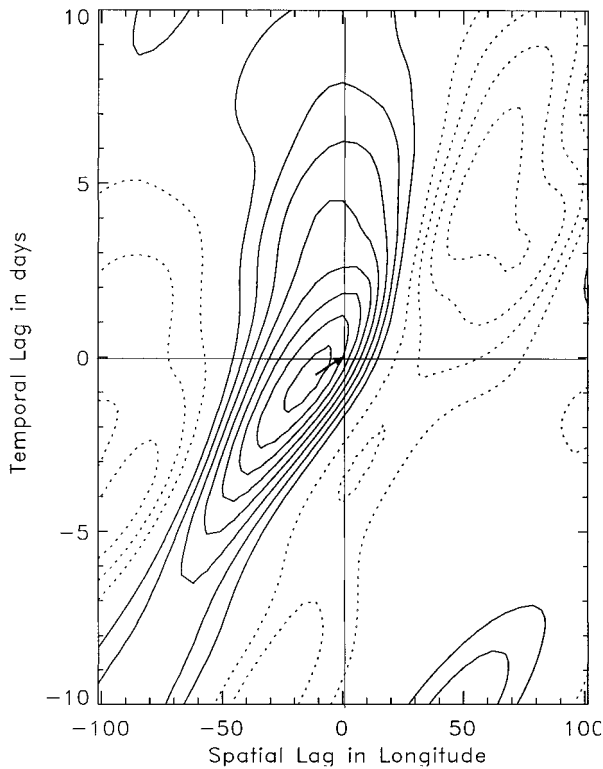


FIG. 11. A contour plot showing the space- and time-lagged correlations between the principal components of EOF2 and the flux index i . The arrow points from the position of maximum correlation to the center point with zero space and time lag. The dataset with 6-hourly data was used and the correlations plotted are averaged between the Northern Hemisphere and (minus) the Southern Hemisphere results.

critical-layer theory to argue that the equatorward flux of wave activity in the late stages of the LC1 was allowed by critical-layer absorption, whereas the largely poleward fluxes in LC2 were associated with nonabsorption or reflection. Second, plots of linear quasigeostrophic refractive index were used to argue using ray theory (e.g., Karoly and Hoskins 1982) that in the LC2 cycle the waves are refracted poleward, away from a minimum in refractive index on the equatorward side of the jet. This minimum was absent in the LC1 case.

THM (section 8) argue, from the wave activity re-

lation of Haynes (1988, Eq. 3.12), that bounds on the time-integrated flux of wave activity into the critical-layer region on the equatorward flank of the jet apply if one assumes small Rossby number scaling and inviscid flow. These bounds allow us to emphasize certain properties of such an idealized nonlinear critical layer. First, if the PV gradient $Q_\phi = 0$ everywhere within the critical layer for a given period, then there can be no net flux of wave activity into the critical layer during this period (see also Killworth and McIntyre 1985), and the layer would reflect. Second, if Q_ϕ is everywhere positive within the critical layer, and the critical layer is relatively undisturbed initially, then subsequent mixing in the critical layer will necessarily be associated with an equatorward flux (absorption).

As the flux index i is strongly dependent on the flux of wave activity into the critical layer on the equatorward side of the jet, a firm theoretical footing for the interpretation of Fig. 7 is possible: reflection must occur when $Q_\phi \approx 0$ to the equatorward side of the jet; this is true in the upper panel, and because it is the $i > 1$ (poleward radiating) composite, reflection is indeed taking place. Conversely, absorption may occur only when Q_ϕ is nonzero, and this is true of the lower panel, which is the $i < -1$ (equatorward radiating) composite. However, for the above arguments, which link fluxes to the rate of change of wave activity, to be valid, the following conditions must be satisfied.

- 1) Dissipation must not be important on the timescale we are considering. This will be true for the radiative damping provided the timescale we are considering is less than r^{-1} . If we use scaling arguments to estimate the scale of the critical layer (e.g., Killworth and McIntyre 1985) as $\Delta y = a\epsilon^{1/2}\Lambda/Q_\phi^0 \approx 1200$ km where $\Lambda \approx 2$ days $^{-1}$, $Q_\phi^0 \approx 10$ days $^{-1}$, and $\epsilon \approx 1$ are the basic-state (time mean) wind shear, quasigeostrophic PV gradient, and the nondimensional wave amplitude, respectively, we can then estimate the overturning timescale of the “Kelvin cat’s-eye” flow in the critical layer as $\Lambda^{-1}k^{-1}\Lambda y^{-1} \approx 1.5$ days, which is much less than r^{-1} . The hyperdiffusion acts on a longer timescale than this only on total wavenumbers less than around 30, and due to the shape of the quasigeostrophic potential vorticity spectra,

TABLE 1. A table showing the values of the maximum and instantaneous correlations between the principal components of EOF2 and the flux index i , as well as the space and time lags of the position of the maximum. Both Northern and Southern Hemisphere results are shown for all four 100-day periods. The periods marked with (*) are the datasets sampled every 6 h; the others are sampled every day.

100-day period	Hemisphere	Instantaneous correlation	Max correlation	Spatial lag	Temporal lag
1*	Northern	0.460	0.532	-11.25°	-12 h
1*	Southern	-0.246	-0.315	-22.5°	-24 h
2	Northern	0.236	0.447	-33.75°	-2 days
2	Southern	-0.266	-0.275	-11.25°	-1 day
3	Northern	0.276	0.373	-11.25°	—
3	Southern	-0.393	-0.426	-5.63°	—
4	Northern	0.318	0.348	-5.63°	—
4	Southern	-0.383	-0.394	-5.63°	—

TABLE 2. Details of the model parameter tests. The run marked † corresponds to the standard run, and that marked ‡ corresponds to a low-resolution (T21) experiment.

Radiative relaxation timescale r^{-1} (days)	Lower boundary drag timescale κ_M^{-1} (days)	Maximum strength of time-mean jet	Location of jet maximum	EOF1 percentage of u^e variability	EOF2 percentage of u^e variability
†25	0.5	33.64 m s ⁻¹	47.10°N	34.04%	24.25%
25	0.3	38.47 m s ⁻¹	44.33°N	39.34%	19.10%
25	1	40.92 m s ⁻¹	47.10°N	34.83%	21.78%
50	0.5	31.04 m s ⁻¹	49.87°N	31.09%	25.14%
15	0.5	38.74 m s ⁻¹	44.33°N	44.30%	17.74%
‡25	0.5	30.81 m s ⁻¹	44.33°N	45.94%	29.89%

these higher wavenumbers do not make a large contribution to the dissipation of wave activity (proportional to $q^e \nabla^8 \psi^e$).

- 2) The advection of wave activity by the mean meridional circulation must not be significant. This must be small for the meridional component of the Haynes wave activity flux to be comparable with $F^{(\phi)}$ in (7). In the upper troposphere of the model, the Eulerian mean meridional velocity does not exceed 3 m s⁻¹ poleward of 20°, suggesting a longer timescale for advection. However, it is possible that a much stronger and more realistic Hadley circulation might have an important effect.
- 3) The divergence of the horizontal component of wave activity flux *within* the critical layer $\int_{\phi_1}^{\phi_2} (a \cos \phi)^{-1} F_\lambda^{(\lambda)} d\phi$ is negligible. This is equivalent to assuming that zonally averaged nonlinear critical-layer theory can also be applied locally in longitude. There is no a priori reason why this should be the case, since in principle wave activity could propagate within the critical layer itself, in the longitudinal direction away from the location where the wave breaking is concentrated initially. Brunet and Haynes (1996) have recently considered this issue in a series of numerical experiments in a barotropic model. They studied Rossby waves generated by a zonally isolated source in midlatitudes and showed that, after an initial period of absorption, wave activity was reflected from the critical-layer region in the subtropics back into midlatitudes, and did not propagate longitudinally within the critical layer.

The linear quasigeostrophic refractive index n^2 could prove to be useful in determining the proportion of wave activity that is initially refracted poleward at the jet center, where the waves are nonbreaking (see also Hartmann and Zuercher 1998). However, we believe it may be misleading to apply this diagnostic to a flow in which wave breaking and mixing are ongoing processes. Consider the analytical solution developed by Stewartson (1978) and Warn and Warn (1978) for a nonlinear Rossby wave critical layer. They used matched asymptotic expansions to derive a limiting case of the 2D vorticity equations in which nonlinear wave breaking is confined

to a thin critical layer. The critical layer was shown to oscillate between an absorbing state and an overreflecting state, eventually settling down to become a perfect reflector. This behavior is not necessarily inconsistent with linear wave theory as vorticity mixing within the critical layer can create a “turning line” (where $Q_y = 0$, so that $n^2 = 0$ in this case) within the critical layer, indicating linear reflection. However, in practice this line will be so close to the critical line (where $u - c = 0$, and $n^2 = \infty$) that it will be difficult to identify. This seems to preclude even the simplest averaging operation of n^2 , as the averages will naturally be dominated by contributions from the critical line, which in practice may not be stationary in space.

The spatial and temporal lag associated with the maximum correlation between the phase of EOF2 and the flux index i is suggestive of a causal link between the changes in the local background flow and the changes in the direction of the meridional flux. The fact that the phase precedes the index suggests that the baroclinic eddies respond to changes in the background flow. Also, the velocity associated with the spatial and temporal lag is of the order of the group velocity of the baroclinic waves, and this leads us to the hypothesis that the eddies adjust to the background flow as they radiate downstream. Of course, the convergence of the wave activity fluxes associated with the eddies must also feed back on the background flow, but there is no locally valid analog to the zonal mean theory of wave-mean flow interaction to indicate precisely how this would work. In fact, such interaction is likely to be complicated, with free modes of the system likely to be excited by forcing with the appropriate wavenumber and frequency. This may account for the propagating long waves seen in Fig. 9c.

9. Summary and conclusions

In this paper we have studied the statistically steady state obtained in a simple, idealized, symmetrically forced primitive equation model of the troposphere. Transient baroclinic eddies were found to be ubiquitous throughout the integration, with amplitudes and phase speeds typical of Southern Hemisphere observations.

These eddies were organized in groups or wave packets that radiated eastward slightly more slowly (at $\approx 25 \text{ m s}^{-1}$) than the wind speed at the jet maximum (33 m s^{-1}). Wave breaking occurred on both sides of the extratropical jet, and could be compared to the four paradigms suggested by Peters and Waugh (1996, PW).

A wave activity flux was then defined to diagnose wave propagation. Based on the meridional component of this flux, an index i was defined to be positive in poleward radiating (PR) regions and negative in equatorward radiating (ER) regions. It was then shown that i was almost always negative at the initiation of an anticyclonic wave breaking event, and positive at the initiation of a cyclonic event, explicitly illustrating the link between meridional propagation and wave breaking suggested by initial value experiments such as those of THM. The local relationship between i and the background flow was then investigated in detail. Composite pictures showed that ER regions (with $i < -1$) were associated with a broad weak jet, displaced slightly poleward relative to the time mean, and with relatively strong potential vorticity gradients in the usually well-mixed region on its equatorward flank. By contrast, PR regions (with $i > 1$) generally coincided with a sharp, strong jet, with very weak (or negative, in the case $i > 1.5$) PV gradients on the equatorward flank. Nonlinear critical-layer theory (e.g., Killworth and McIntyre 1985) provides a theoretical framework in which to view this behavior, as any region in which the PV is homogenized must remain a perfect reflector of wave activity for all time.

These results are consistent with those of Akahori and Yoden (1997). When the *zonal mean* jet in their model experiment was perturbed by a structure similar to that of Fig. 6a (i.e., the negative phase of their EOF1), they showed that cyclonic breaking was more likely than anticyclonic. In the positive phase of their EOF1, anticyclonic breaking was more prevalent. Perhaps surprisingly, however, the results presented here seem to be somewhat at odds with those in Lee and Feldstein (1996), who show that in their GCM experiment equatorward EP fluxes are associated with sharper, slightly poleward displaced jet (see their Figs. 5j, 12c), and poleward fluxes with a broader, weaker, equatorward displaced jet. However, as argued in section 8, we believe that it is the distribution of the potential vorticity field that is ultimately more important in determining the direction of the wave activity fluxes. As the dynamics of Lee and Feldstein's experiment are somewhat different, and they do not show any PV plots, it is difficult to draw any firm conclusions about this apparent difference.

In section 6 we then went further than the above studies to investigate the full spatial and temporal relationship between background zonal flow structure and the sense of the flux index. A cross-sectional EOF study (see Esler 1997) was applied to the full zonal wind field u to explicitly study the internal variability of the tro-

pospheric circulation. The first EOF was extremely well correlated with the baroclinic waves, as measured by meridional velocity, effectively filtering these out, and allowing us to investigate the remaining variability with the remaining EOFs. The second EOF was the only remaining one to describe significant variance, and it was found to have structure in the latitude–height plane very similar to the difference in the composites between the PR and ER regions. The principal components of the second EOF showed that it also propagated in a wavelike manner, but with frequency (≈ 11 – 14 days), wavelength (wavenumbers 2–4), and angular phase speed ($\approx 0.1 \text{ days}^{-1}$) distinct from those of the baroclinic waves. In particular, individual phase maxima of these waves persisted for up to ≈ 20 – 25 days, in contrast to the baroclinic waves for which wave activity is quickly radiated downstream (e.g., Chang 1993). The phase of these waves was then shown to be correlated with the flux index, with the maximum correlation occurring at a space and time lag, indicating that the flow structure precedes the maximum response in the flux index. This also shows that it is the local structure of the background zonal flow that influence the direction of wave breaking, not merely the zonal mean wind, as shown by Akahori and Yoden (1997).

These waves are perhaps most likely to be free modes of the system, excited by the variability of the baroclinic waves themselves. This hypothesis might be tested by a detailed investigation of the response of a zonally symmetric atmosphere to forcing due to the zonally localized potential vorticity fluxes associated with wave packets. The waves themselves, apart from influencing the propagation of the baroclinic eddies, may be a substantial source of transient waves in the stratosphere, particularly in the Southern Hemisphere where eastward-propagating wave 2 can often reach large amplitudes [see, e.g., Manney et al. (1991) and the modeling study by Scinocca and Haynes (1998)].

It is perhaps surprising that so much of the variability that controls the wave breaking takes place on a length scale that is significantly shorter than the packet length scale. Typically the EOF2 waves have a length scale corresponding to wavenumber 3, which means that the wave packets, when viewed on a pressure surface, often have an arc shape or “S” shape (see Fig. 3). Of course, this is hardly likely to be the case in a model in which realistic zonal asymmetries have been imposed, but in such a model it may be the case that stationary waves that influence the meridional shear of the jet can be shown to have a similar effect to EOF2. In any case, an understanding of the *internal* mechanism that gives rise to variability in wave breaking is a vital starting point in understanding the variability of this process in the real atmosphere.

Acknowledgments. This work was done partly at the University of Cambridge with financial support of the Natural Environment Research Council (United King-

dom) and the U.K. Meteorological Office through a CASE research studentship and with additional support from U.K. Universities Global Atmospheric Modelling Programme. The work was completed and written up at the Massachusetts Institute of Technology under NSF Grant 9528471-ATM. Helpful discussions with Alan Plumb, Lorenzo Polvani, and Edmund Chang, as well as comments and proofreading by Tieh Yong Koh, are gratefully acknowledged

REFERENCES

- Akahori, K., and S. Yoden, 1997: Zonal flow vacillation and bimodality of baroclinic eddy life cycles in a simple global circulation model. *J. Atmos. Sci.*, **54**, 2349–2361.
- Appenzeller, C., and H. C. Davies, 1992: Structure of stratospheric intrusions into the troposphere. *Nature*, **358**, 570–572.
- , —, and W. A. Norton, 1996: Fragmentation of stratospheric intrusions. *J. Geophys. Res.*, **101**, 1435–1456.
- Brunet, G., and P. H. Haynes, 1996: Low-latitude reflection of Rossby wave trains. *J. Atmos. Sci.*, **53**, 482–496.
- Chang, E. M., 1993: Downstream development of baroclinic waves as inferred from regression analysis. *J. Atmos. Sci.*, **50**, 2038–2053.
- Edmon, H. J., B. J. Hoskins, and M. E. McIntyre, 1980: Eliassen–Palm cross sections for the troposphere. *J. Atmos. Sci.*, **37**, 2600–2616; Corrigendum, **38**, 1115.
- Esler, J. G., 1997: Wave packets in simple equilibrated baroclinic systems. *J. Atmos. Sci.*, **54**, 2820–2849.
- , and P. H. Haynes, 1999: Mechanisms for wave packet formation and maintenance in a quasigeostrophic two-layer model. *J. Atmos. Sci.*, **56**, 2457–2490.
- Hartmann, D. L., 1995: A PV view of zonal flow vacillation. *J. Atmos. Sci.*, **52**, 2561–2576.
- , and P. Zuercher, 1998: Response of baroclinic life cycles to barotropic shear. *J. Atmos. Sci.*, **55**, 297–313.
- Haynes, P. H., 1988: Forced, dissipative generalizations of finite-amplitude wave-activity conservation relations for zonal and non-zonal basic flows. *J. Atmos. Sci.*, **45**, 2352–2362.
- Held, I. M., and P. J. Phillips, 1990: A barotropic model of the interaction between the Hadley cell and a Rossby wave. *J. Atmos. Sci.*, **47**, 856–869.
- Hoskins, B. J., H. H. Hsu, I. N. James, M. Masutani, P. D. Sardeshmukh, and G. H. White, 1989: Diagnostics of the global atmospheric circulation. World Climate Report Programme - 27, WMO/TD 326, 89 pp. and 121 plates.
- Karoly, D. J., and B. J. Hoskins, 1982: Three-dimensional propagation of planetary waves. *J. Meteor. Soc. Japan*, **60**, 109–123.
- Killworth, P. D., and M. E. McIntyre, 1985: Do Rossby-wave critical layers absorb, reflect or over-reflect? *J. Fluid Mech.*, **161**, 449–492.
- Lee, S., and I. M. Held, 1993: Baroclinic wave packets in models and observations. *J. Atmos. Sci.*, **50**, 1413–1428.
- , and S. Feldstein, 1996: Two types of wave breaking in an aquaplanet GCM. *J. Atmos. Sci.*, **53**, 842–857.
- Magnusdottir, G., and P. H. Haynes, 1996: Wave activity diagnostics applied to baroclinic wave life cycles. *J. Atmos. Sci.*, **53**, 2317–2353.
- Manney, G. L., J. D. Farrara, and C. R. Mechoso, 1991: The behavior of wave 2 in the Southern Hemisphere stratosphere during late winter and early spring. *J. Atmos. Sci.*, **48**, 976–998.
- McIntyre, M. E., and T. N. Palmer, 1984: The “surf zone” in the stratosphere. *J. Atmos. Terr. Phys.*, **46**, 825–849.
- , and —, 1985: A note on the general concept of wave breaking for Rossby and gravity waves. *Pure Appl. Geophys.*, **123**, 964–975.
- Peters, D., and D. W. Waugh, 1996: Influence of barotropic shear on the poleward advection of upper tropospheric air. *J. Atmos. Sci.*, **53**, 3013–3031.
- Plumb, R. A., 1985: On three-dimensional propagation of stationary waves. *J. Atmos. Sci.*, **42**, 217–229.
- Scinocca, J. F., and P. H. Haynes, 1998: Dynamical forcing of stratospheric planetary waves by tropospheric baroclinic eddies. *J. Atmos. Sci.*, **55**, 2361–2392.
- Simmons, A. J., and B. J. Hoskins, 1980: Barotropic influences on the growth and decay of nonlinear baroclinic waves. *J. Atmos. Sci.*, **37**, 1679–1684.
- Stewartson, K., 1978: The evolution of the critical layer of a Rossby wave. *Geophys. Astrophys. Fluid Dyn.*, **9**, 185–200.
- Swanson, K. L., P. J. Kushner, and I. M. Held, 1997: Dynamics of barotropic storm tracks. *J. Atmos. Sci.*, **54**, 791–810.
- Thorncroft, C. D., B. J. Hoskins, and M. E. McIntyre, 1993: Two paradigms of baroclinic life cycle behaviour. *Quart. J. Roy. Meteor. Soc.*, **119**, 17–35.
- Vanneste, J., and T. G. Shepherd, 1998: On the group velocity property for conservation laws. *J. Atmos. Sci.*, **55**, 1063–1068.
- Warn, T., and H. Warn, 1978: The evolution of a nonlinear critical level. *Stud. Appl. Math.*, **59**, 37–71.